# Exploration of the Structural Features Defining the Conduction Properties of a Synthetic Ion Channel

Gregg R. Dieckmann,* James D. Lear,* Qingfeng Zhong,# Michael L. Klein,# William F. DeGrado,* and Kim A. Sharp*

*The Johnson Research Foundation, Department of Biochemistry and Biophysics, University of Pennsylvania, Philadelphia, Pennsylvania 19104-6059, and #Center for Molecular Modeling and Department of Chemistry, University of Pennsylvania, Philadelphia, Pennsylvania 19104-6323 USA

ABSTRACT The finite-difference Poisson-Boltzmann methodology was applied to a series of parallel, $\alpha$-helical bundle models of the designed ion channel peptide Ac-$(LSSLLSL)_3$-$CONH_2$. This method is able to fully describe the current-voltage curves for this channel and quantitatively explains their cation selectivity and rectification. We examined a series of energy-minimized models representing different aggregation states, side-chain rotamers, and helical rotations, as well as an ensemble of structures from a molecular dynamics trajectory. Potential energies were computed for single, permeating $K^+$ and $Cl^-$ ions at a series of positions along a central pathway through the models. A variable-electric-field Nernst-Planck electrodiffusion model was used, with two adjustable parameters representing the diffusion coefficients of $K^+$ and $Cl^-$ to scale the individual ion current magnitudes. The ability of a given DelPhi potential profile to fit the experimental data depended strongly on the magnitude of the desolvation of the permeating ion. Below a pore radius of 3.8 Å, the predicted profiles showed large energy barriers, and the experimental data could be fit only with unrealistically high values for the $K^+$ and $Cl^-$ diffusion coefficients. For pore radii above 3.8 Å, the desolvation energies were $2kT$ or less. The electrostatic calculations were sensitive to positioning of the Ser side chains, with the best fits associated with maximum exposure of the Ser side-chain hydroxyls to the pore. The backbone component was shown to be the major source of asymmetry in the DelPhi potential profiles. Only two of the energy-minimized structures were able to explain the experimental data, whereas an average of the dynamics structures gave excellent agreement with experimental results. Thus this method provides a promising approach to prediction of current-voltage curves from three-dimensional structures of ion channel proteins.

## INTRODUCTION

Ionic conduction through transmembrane protein pores in cell membranes is a highly regulated process in living systems (Hille, 1992). Much of this regulation is at the level of individual protein molecules, many of which show remarkable selectivity in conducting different, physiologically important metal ions. Many essential ion channel proteins have been sequenced, and their conserved sequence features have been correlated with their conduction properties (Imoto, 1993; Sather et al., 1994; Yool and Schwartz, 1991). The three-dimensional structures of several channels, including gramicidin (Roux and Karplus, 1994), porin (Weiss et al., 1991, Weiss and Schulz, 1992) and the newly solved potassium channel (Doyle et al., 1998), have been reported. However, predicting ionic currents from three-dimensional protein structures is very challenging, particularly for those channels with the small pore radii ($<5$ Å) characteristic of most ion channels associated with nerve conduction. This challenge arises because the electrostatic energies of charged species are so large, and because the electrostatic influences on permeation of charged species can become very large in confined spaces. For example, the calculated solvation energy of a $K^+$ ion in water versus vacuum is $-76.8$ kcal/mol (Rashin and Honig, 1985). Even a 1% difference ($\sim RT$) in solvation energy produced by transferring the ion from bulk water to the pore would have a significant effect on permeation. In general, when an ion is transferred from an isotropic medium to one of the same dielectric constant—but which is surrounded by one of lower dielectric constant—ion transfer energies far in excess of thermal energies can result (Parsegian, 1969). The magnitude of the energies is largely dependent on the size and shape of the dielectric boundary (Parsegian, 1975).

A number of powerful computational methods are now available to calculate electrostatic potential fields from very complex, discrete distributions of charges embedded in media of discontinuous dielectric constant (Cortis and Friesner, 1997; Gilson et al., 1988; Sharp and Honig, 1990). Moreover, these methods are beginning to be applied to the calculation of ion permeation rates in static (Woolley et al., 1997) and dynamic (Hao et al., 1997; Smith and Sansom, 1997) models of natural ion channels.

Our interest has focused on understanding the ion conduction properties of LS3, a designed amphiphilic $\alpha$-helical peptide with the sequence Ac-$(LSSLLSL)_3$-$CONH_2$. LS3 has been shown to form voltage-gated channels composed of parallel helical aggregates when incorporated into planar lipid bilayers, and single-channel conductance measurements indicate that LS3 displays both current rectification and a $\sim$10-fold selectivity for cations (Åkerfeldt et al.,

*Received for publication 30 June 1998 and in final form 20 October 1998.*

Address reprint requests to Dr. Kim A. Sharp, Department of Biochemistry and Biophysics, University of Pennsylvania, Anatomy and Chemistry Building, Room 417, 37th and Hamilton Walk, Philadelphia, PA 19104-6059. Tel.: 215-573-3506; Fax: 215-898-4217; E-mail: sharpk@mail.med.upenn.edu.



0006-3495/99/02/618/13 $2.00

1995; Lear et al., 1988). The ability of LS3 to give measurable single-channel conductance for cations as large as $Tris^+$, but not glucosammonium, suggests that LS3 has a pore size of ~4 Å radius, placing LS3 in the group of channels with midsized pores. This group includes the cation-selective nicotinic receptor, with a 3.5–4.0-Å pore radius (Cohen et al., 1992; Dwyer et al., 1980) and the anion-selective $GABA_A$ and glycine receptors, with pore radii of ~3 Å (Bormann et al., 1987; Fatima-Shad and Barry, 1993). The structural simplicity of LS3 makes it a particularly attractive model for studying the current-voltage (*IV*) characteristics of this class of proteins. It contains an exact heptad repeat that should induce a structurally regular multistranded coiled coil with a pore of uniform diameter. Of all elements of protein structure—in soluble as well as in membrane proteins—the coiled coil is the most accurately predicted and modeled (Crick, 1953; Dieckmann and DeGrado, 1997; Dunker and Zaleske, 1977; Kohn et al., 1997; Pauling et al., 1951; Woolfson and Alber, 1995).

In an attempt to model the cation selectivity and rectification displayed by LS3 (Kienker et al., 1994) and derivatives of this peptide (Lear et al., 1997), we previously used a continuum electrodiffusion model together with a simplified geometric model containing point charges radially arranged around a cylindrical pore. Data in symmetrical KCl solutions (indicating that the bath solutions on the two sides of the channel contain the same salt concentration) were well described by a pore with a radius of 4 Å and a length of 30 Å and physically reasonable adjustable parameters involving ion permeabilities, pore/wall dielectric constants, and screened end charges. However, data in asymmetric salt solutions (Kienker and Lear, 1995) were fit less satisfactorily, and the observed charge selectivity could not be explained by any of the theoretical parameters. Mathematical modeling with a kinetic model for transitions among ion-occupied and empty states allowed fitting of the data but required 13 adjustable parameters of doubtful physical significance (Kienker and Lear, 1995). Application of Poisson-Nernst-Planck (PNP) theory (Chen et al., 1992) fit the data reasonably well with only four parameters (Chen et al., 1997), but the best-fit value of the $\alpha$-helix end charge was only 5% of its generally accepted value (Sitkoff et al., 1994). Furthermore, this theory predicted that the observed cation selectivity arose from an eightfold larger diffusion coefficient for $K^+$ versus $Cl^-$ within the channel, a result that is difficult to reconcile with molecular models of the channel. To summarize, these previous studies were able to account to some degree for the rectification and selectivity properties of LS3, but because they lacked atomic resolution information, it was not possible to analyze in any detail the structural features that give rise to channel conductance properties.

To overcome this limitation, we sought a theoretical method that would utilize the information contained in detailed molecular structures to predict channel properties. In this article we report the application of the finite-difference Poisson-Boltzmann (FDPB) methodology (Sharp and Honig, 1990) to compute the potential energies of $K^+$ and $Cl^-$ ions (relative to bulk water) at discrete positions within a permeation pathway defined through the center of pores formed by $\alpha$-helical bundles of LS3. Rather than focusing on a single model, we examined a series of reasonable models obtained using energy minimization or molecular dynamics calculations. Experimental results indicate that the most reasonable aggregation state for this channel is six or seven (Åkerfeldt et al., 1993). Therefore, we examined models composed of five to eight helices. The potential energy profiles for each model were then calculated using Nernst-Planck (NP) electrodiffusion theory to fit experimental data with parameters to scale the magnitudes of the observed current. The structural details of how simple bundles of $\alpha$-helices give rise to the specific channel properties observed for LS3 will be discussed. (We used NP instead of PNP theory because PNP does not appear to be as applicable to the single ion transit situation postulated in this work. NP and PNP are continuum electrodiffusion theories that use the same differential equation to compute current from the electrical potential. The major difference between the two theories is that in PNP the potential itself depends on the magnitude of the current; as the current increases, the density of charge inside the channel also increases, changing the potential. However, ions are discrete charges, and because we postulate single ion occupancy, it seems inconsistent to employ a theory that effectively requires the channel to retain a "memory" of the passage of previous ions.)

## METHODS

### Model building

The methods used for the mathematical generation of helical bundles have been described previously (Betz and DeGrado, 1996, Dieckmann, 1995; Dieckmann 1998; Shen et al., 1996). To model LS3 as an ion channel, an ideal helix was built with the program Insight95 (Biosym/Molecular Simulations, San Diego, CA) with the sequence Ac-(LSSLLSL)$_3$-$CONH_2$. Ser and Leu side chains were placed into one of two low-energy rotamers (Ser $g+$: $\chi_1 = 60°$; Ser $g-$: $\chi_1 = -60°$; Leu $g+$: $\chi_1 = -60°$, $\chi_2 = -175°$; Leu $t$: $\chi_1 = -175°$, $\chi_2 = 75°$) (Dunbrack and Cohen, 1997; Dunbrack and Karplus, 1994; McGregor et al., 1987). Three helices with different combinations of Ser and Leu $\chi_1$ rotamers were built: $g+$ for both Ser and Leu; $g+$ for Ser and $t$ for Leu; or $g-$ for Ser and $g+$ for Leu. Each helix was transformed to 3.5 residues per turn, using a matrix transformation (Equation 1 in Dieckmann, 1998)

$$\begin{pmatrix} x_{new}(i) \\ y_{new}(i) \\ z_{new}(i) \end{pmatrix} = \begin{bmatrix} \cos(\theta) & -\sin(\theta) & 0 \\ \sin(\theta) & \cos(\theta) & 0 \\ 0 & 0 & 1 \end{bmatrix} \begin{bmatrix} x(i) \\ y(i) \\ z(i) \end{bmatrix} \quad (1)$$

where $\theta = -2\pi z(i)/p$, with a superhelical pitch ($p$) of $-189$ Å. Next, symmetrical helical bundles with aggregation states from five to eight helices were generated by varying

$r$ (the distance of the helix from the bundle center) and $\epsilon$ (the rotation of each helix around its axis, which defines the residues that point toward the bundle center) (Fig. 1 *A*) and applying the appropriate symmetry operator. Two different values for $\epsilon$ were used: the first rotation ($\epsilon_A$) orients the $\alpha$-helices in a classical coiled coil with the register ($Leu_c$-$Ser_d$-$Ser_e$-$Leu_f$-$Leu_g$-$Ser_a$-$Leu_b$), in which the subscripts designate the positions in the heptad repeat. This alignment places the first and third Ser (at d and a positions) of each heptad within the channel (Fig. 1 *A*); the second Ser (at position e) adopts a more interfacial position at the helix/helix boundary. A second rotation ($\epsilon_B$) involves an additional rotation about the helical axis of ~20°. As previously discussed by Dunker (Dunker and Zaleske, 1977), this alignment positions the side chains of residues at d, e, and a within the pore while maintaining good side-chain packing at the remaining positions (Fig. 1 *B*). Thus this alignment maximizes the solvation of all three Ser residues within the central pore.

The helical bundles were given a left-handed twist, using equation 1 of Dieckmann et al. (1998) with a $p$ of either 189 Å (for pentamers and hexamers) or 350 Å (for heptamers and octamers; the large value of $p$ was used to prevent excessive curvature of the helices in these bundles; Dunker and Zaleske, 1977). The parameters used in the construction of models are listed in Table 1. For each channel model, the SOAK command in Insight95 was used to place water molecules in the channel pore as well as in a 5-Å-thick layer at the N- and C-termini of the channels. No water molecules were placed on the hydrophobic exteriors of the bundles. The resulting models were subjected to energy minimizations using Discover (Biosym/Molecular Simulations) and the CVFF force field (Dauber-Osguthorpe et al., 1988). The energy-minimized models displayed reasonable helix/helix packing interactions and maintained in general the helical rotations and bundle symmetries used to build the structures (Fig. 1).

**TABLE 1 Nomenclature for molecular models**

| Model | Ser rotamer* | Leu rotamer* | Helix/helix distance (Å) | $\epsilon^{\#}$ |
|---|---|---|---|---|
| G9 | $g+$ | $g+$ | 9 | A |
| G10 | $g+$ | $g+$ | 10 | A |
| GB9 | $g+$ | $g+$ | 9 | B |
| GB10 | $g+$ | $g+$ | 10 | B |
| T9 | $g+$ | $t$ | 9 | B |
| T10 | $g+$ | $t$ | 10 | B |
| GM10 | $g-$ | $g+$ | 10 | B |

*$\chi_1$ side-chain rotamer.
#Helical rotation used in the model building procedure. $\epsilon_A$ placed the three Ser residues of each heptad repeat into the *a*, *d*, and *e* positions of a classical coiled-coil heptad repeat. $\epsilon_B$ is a 20° counterclockwise rotation (with respect to $\epsilon_A$).

The dynamic hexameric models were generated from unrestrained molecular dynamics calculations performed on a model channel of LS3 in a membrane mimetic environment (Zhong et al., 1998). Structures for DelPhi calculations were selected at 6-ps intervals after an equilibration time of ~3 ns and represent the magnitude of the structural fluctuations observed for the equilibrated channel. Water and octane molecules were removed from all models before performing DelPhi calculations.

## Electrostatic calculations

For each model of the LS3 ion channel, the electrostatic energy was calculated for the process of moving an ion ($K^+$ or $Cl^-$) through the channel pore from the N-terminal side (N-side) to the C-terminal side (C-side) of the channel. The

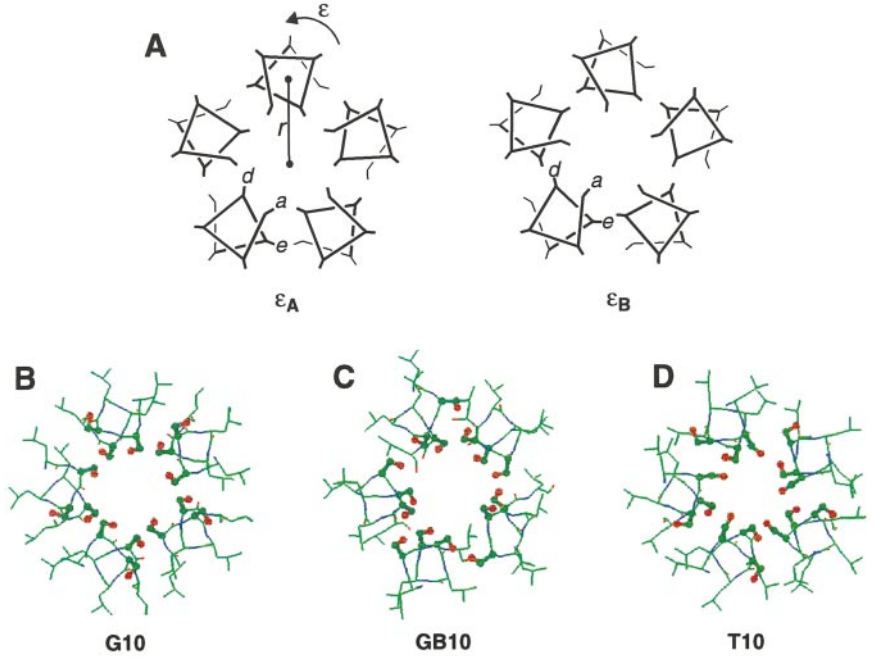


FIGURE 1 Important features of the modeling procedure for LS3 (pentamer models). (*A*) Schematic illustrating the positions of the Ser residues with respect to the channel pore for $\epsilon_A$ (*left*) and $\epsilon_B$ (*right*) (see Table 1 for nomenclature). $r$ is the distance of each helix from the bundle center; this value is adjusted to obtain the desired helix/helix distance. $\epsilon_A$ or $\epsilon_B$ is the helical rotation used to position the Ser residues with respect to the channel pore. For $\epsilon_B$, an additional rotation of 20° counterclockwise with respect to $\epsilon_A$ was used for each helix. The labels *a*, *d*, and *e* designate Ser positions in a classical heptad repeat of a coiled coil. Leu residues are not shown for clarity. (*B–D*) Single heptad slices (viewed from the N-terminus) of the energy-minimized G10 (*B*), GB10 (*C*), and T10 (*D*) pentamer models. Ser side chains are shown as ball-and-stick representations. Atom colors: green, carbon; red, oxygen; blue, nitrogen.

ion channel model was centered at the origin with the pore aligned along the *z* axis of the Cartesian coordinate system and inserted into a 34-Å-thick slab of close-packed dummy atoms that simulates a membrane bilayer. Electrostatic energies were calculated using the FDPB methodology implemented in the software package DelPhi (Gilson et al., 1988; Nicholls et al., 1991; Sharp and Honig, 1990). For the calculations, the grid dimensions were 65 × 65 × 65, with a scale of ~1 grid/Å. Solutions were obtained for the nonlinear Poisson-Boltzmann equation with Coulombic boundary conditions (Gilson et al., 1988), using the multigridding method of iteration (Holst and Saied, 1993; Sharp et al., 1995). For a representative calculation, the system was mapped onto the grid in 64 different positions, and the results were averaged to obtain an estimate of the numerical precision of the calculations. The radii and charge values used are listed in Table 2; similar results were obtained from the OPLS parameter set (Jorgensen and Tirado-Rives, 1988). The solvent and protein dielectric constants were 80 and 2, respectively. The membrane slab had dimensions of 60 Å × 60 Å × 34 Å, with a dielectric constant of 2.0. This slab separates the solvent region into two halves, with the only connection between the two being the pore through the channel.

The DelPhi program was modified to accept asymmetrical salt concentrations on the two sides of the membrane. The solvent region of the system (high dielectric) was divided into three regions by two planes, each parallel to the *xy* plane, that were displaced along the *z* axis (Fig. 2). $Z_N$ defines the *z* axis displacement for the plane separating the N-terminal (N-side) solvent from the pore of the channel; analogously, $Z_C$ is the *z* axis position for the plane between the channel pore and the C-terminal (C-side) solvent region. The values for $Z_N$ and $Z_C$ were defined by the N- and C-terminal ends, respectively, of the ion channel models. The two bulk solvent regions have the same high dielectric,

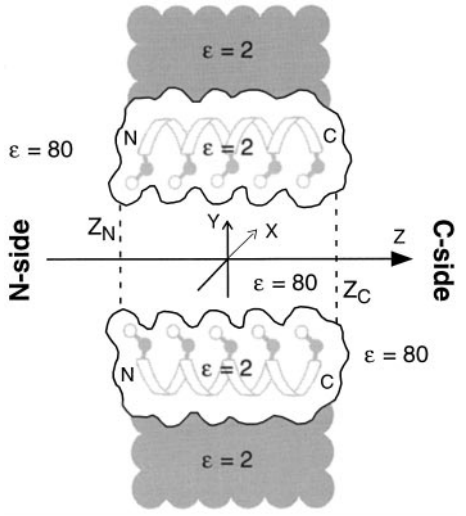


FIGURE 2 Basic components of the ion channel model system. The ion channel (only two of the helices are shown for clarity) is inserted in a membrane mimetic (represented by the *shaded regions*). $Z_N$ and $Z_C$ define the planes that separate the high-dielectric region in the channel pore from the bulk N-terminal (N-side) and C-terminal (C-side) regions, respectively. N and C indicate the N- and C-termini of the helices. The orientation of the model system with respect to the Cartesian coordinate system is indicated.

but separate ion concentrations defined as $[KCl]_N$ and $[KCl]_C$ for the N-side and C-side regions, respectively. Within the pore, a dielectric of 80 and an ionic concentration of zero were used. (The solvent dielectric constant was 80 both inside and outside the pore. The dielectric constant of the pore water primarily affects the calculation of the ion hydration energy. Although some molecular dynamics calculations (Sansom et al., 1997b) show restricted water rotational mobility within pores such as those modeled here, such effects should not have a large influence on the solvation energy of the permeating ion. Permeant ion studies (Lear et al., 1988) indicate that the pore radius of LS3 is large enough to accommodate a $K^+$ ion with at least one or two solvation shells of water (data not shown). It is reasonable to assume that these waters close to the $K^+$ ion will provide as much solvation energy as they would in bulk water.) The permeating ion was treated explicitly by placing the ion at a series of positions within the pore; the ion trajectory was either assumed to be straight along the *z* axis or defined using the HOLE suite of programs (Smart et al., 1996). For all models examined, the two approaches gave essentially identical results.

The electrostatic energy resulting from the interaction of the permeating ion with the channel (and membrane) was computed as the sum of three components (Fig. 3). First, the ion experiences a change in solvation when moving from the bulk solvent phase to the pore of the channel. To determine the energetic consequences of this "desolvation", we computed the self-energy of the ion (Sharp and Honig, 1990) at a given position along the ion trajectory in two different dielectric environments—in bulk solvent only, as well as solvent plus the protein/membrane dielectric re-

**TABLE 2 Atomic charges used for electrostatic calculations**

| Location | Atom | Charge* | Size# |
|---|---|---|---|
| Backbone | N | −0.52 | 1.65 |
| | HN | 0.248 | 0.00 |
| | CA | 0.246 | 1.90 |
| | C | 0.526 | 1.90 |
| | O | −0.5 | 1.60 |
| Ac§ | CA | 0.0 | 1.90 |
| | HA | 0.0 | 0.00 |
| | C | 0.5 | 1.90 |
| | O | −0.5 | 1.60 |
| NH2¶ | HN | 0.26 | 0.00 |
| Ser side chain | CB | 0.25 | 1.90 |
| | OG | −0.65 | 1.60 |
| | HG | 0.4 | 0.00 |
| Ions | $K^+$ | 1 | 2.17 |
| | $Cl^-$ | −1 | 1.94 |

*Charge given in proton charge units.
#Radius given in Å.
§Acetyl group on peptide N-terminus.
¶Amide group on peptide C-terminus.

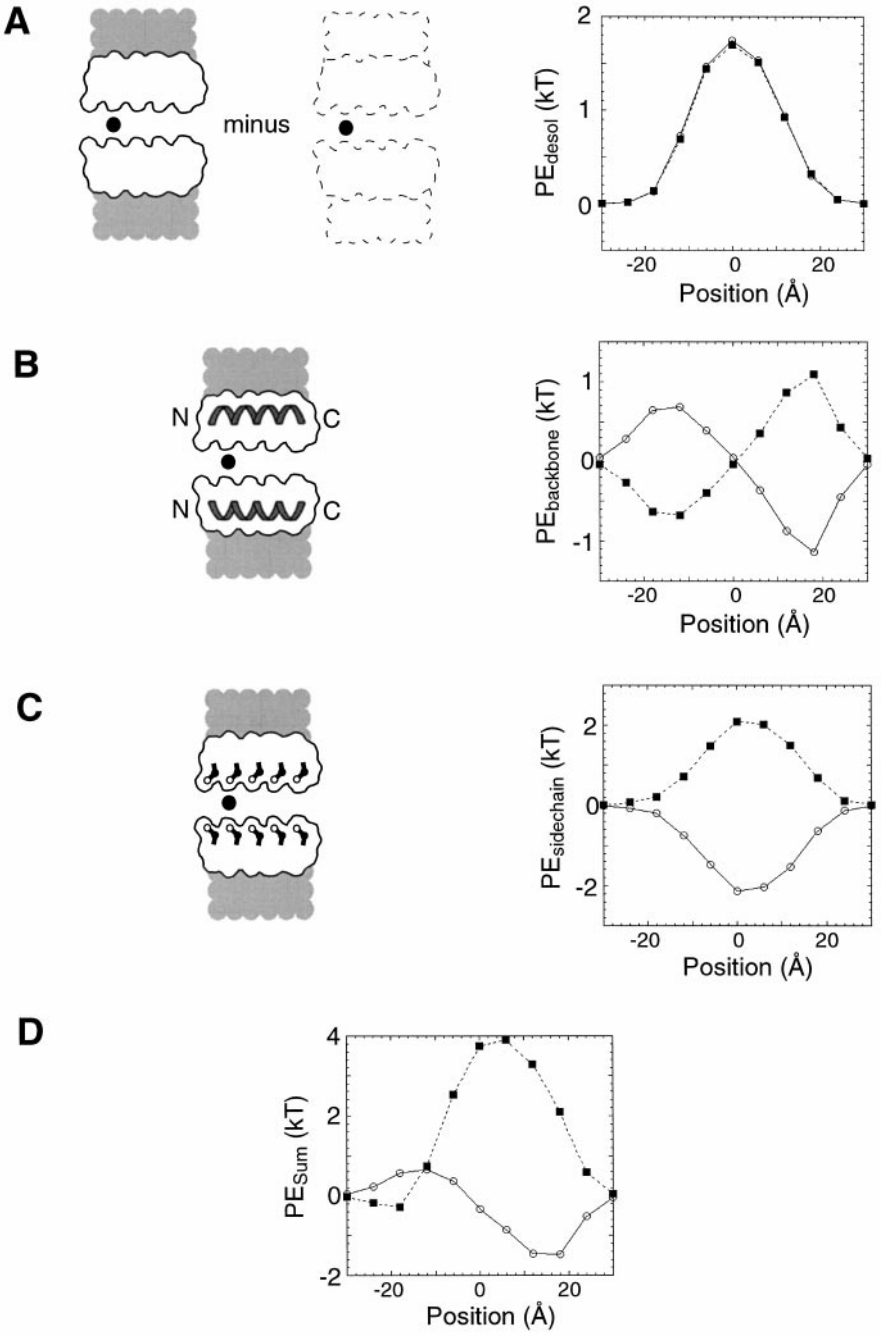


FIGURE 3 Illustration of how potential profiles for permeating ions are calculated, with schematics of the computed interactions on the left, and plots showing the computed potentials on the right (potential energy in $kT$ versus position of ion in channel along the $z$ axis in Å). In the potential profile plots, both $K^+$ (○) and $Cl^-$ (■) potentials are shown. (*A*) Desolvation is computed as the difference between the self-energy of the permeating ion (partial charges of all channel atoms set to zero) in the solvent plus protein/membrane and the solvent-only dielectric environments. The $K^+$ and $Cl^-$ curves overlap. (*B*) Backbone component (partial charges of the sidechain atoms set to zero). (*C*) Ser side-chain component (partial charges of the backbone atoms set to zero). (*D*) Sum of components in *A*–*C*.

gions. For both self-energy calculations, only the charge associated with the permeating ion was used; partial charges of the channel atoms were set at zero. The desolvation energy is then the difference between these two self-energies (Fig. 3 *A*).

Contributions to the electrostatic energy also arise from the interaction of the ion with the atomic partial charges of the ion channel. These contributions were broken down into two categories representing the backbone (Fig. 3 *B*) and side-chain atoms (Fig. 3 *C*). For the calculation of the backbone component, the partial charges of the backbone atoms (N, HN, CA, C and O atoms) were used, and the side-chain atom partial charges were set at zero. For the potential energy due to protein side chains interacting with the permeating ion, the Ser CB, OG, and HG atoms were assigned partial charges, with all other atoms (including all backbone and Leu side-chain atoms) set to zero.

It should be noted that the potential profiles for some of the models display an uneven, or "spiked," shape (as seen, for example, in Figs. 4, 5, and 7 *A*). These abrupt fluctuations in the potentials arise from very localized computed interactions. In nature, the dynamics of the system would adjust in response to these interactions and "smooth out" the potential profiles. Because we compute the integral of the potential when fitting the experimental data (Eq. 2 below), the potential profiles are smoothed by the integration pro-

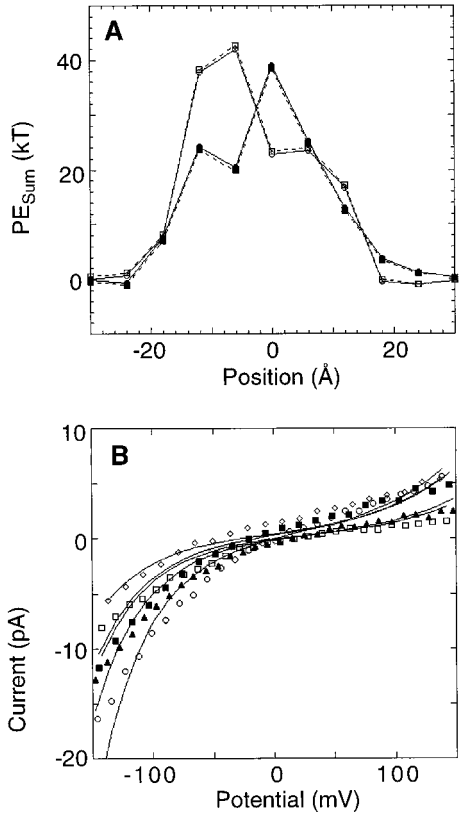


FIGURE 4 Computed potential profiles (*A*) and curves fitted to experimental *IV* data (*B*) for the T10 pentamer model. For the potential profiles, the potential energy (*kT*) is plotted versus the position of the permeating ion in the channel pore (Å) along the *z* axis. Potentials are shown for $K^+$ (◇, □, ○) and $Cl^-$ (■, ▲) with N-side/C-side KCl concentrations of 1.1 M/0.053 M (○, ●) or 0.069 M/1.1 M (□, ■). For the plots showing fitted curves to *IV* data, the solid lines represent the fits and the symbols represent the experimental data for various N-side/C-side KCl concentrations (1.0 M/1.0 M, ○; 1.0 M/0.24 M, ■; 1.1 M/0.053 M, ◇; 0.24 M/1.0 M, ▲; 0.069 M/1.1 M, □).

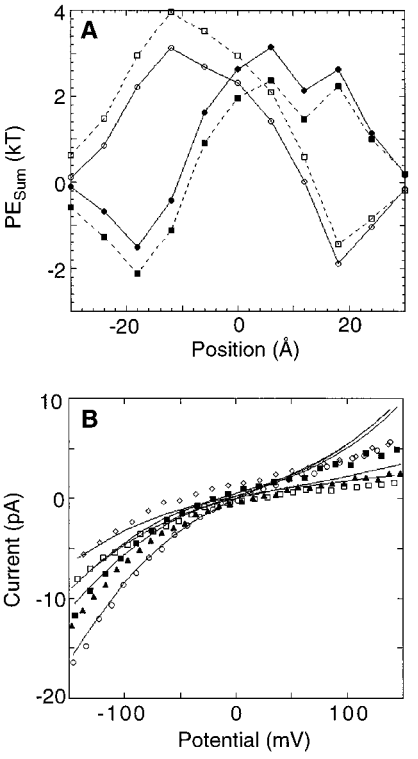


FIGURE 5 Computed potential profiles (*A*) and curves fitted to experimental *IV* data (*B*) for the G9 heptamer model. The symbols are the same as in Fig. 4.

cess (except for the G10 hexamer, where two obviously extreme data points were removed from the calculation). For the MD hexamer, potential energy profiles were computed for each of the six structures from the dynamics trajectory and then averaged together to generate an average profile used to fit the *IV* data (below).

## Use of DelPhi-defined potential profiles to fit current-voltage data

The Nernst-Planck electrodiffusion theory was used to fit experimental single-channel *IV* curves over a wide range of electrolyte activities, using the DelPhi computed ion potential energy profiles. The single-channel current is given by Eq. 2, where

$$I(V) = \pi r^2 F \left\{ \frac{D_K[a_K^N \exp(+VF/RT) - a_K^C]}{\int_{-L/2}^{+L/2} \exp[\phi_K(z, V)F/RT]dz} - \frac{D_{Cl}[a_{Cl}^N \exp(-VF/RT) - a_{Cl}^C]}{\int_{-L/2}^{+L/2} \exp[\phi_{Cl}(z, V)F/RT]dz} \right\} \quad (2)$$

$I(V)$ is the current (amperes) as a function of the transpore voltage ($V$); $r$ is the pore radius as computed by HOLE (see Table 3); $F$ is the Faraday constant ($9.648 \times 10^4$ coulombs/mol); $a_K^N$, $a_K^C$, $a_{Cl}^N$, and $a_{Cl}^C$ are the solution activities in mol/cm$^3$ for $K^+$ or $Cl^-$; $V$ is the applied voltage (V) at $z = -L/2$; $L$, the length of the channel pore, was determined from the models to be $\sim 34 \times 10^{-8}$ cm; $RT$ is the thermal energy (0.0257 eV at 25°C). $\phi_K$ and $\phi_{Cl}$ are the total potentials and are defined in Eqs. 3 and 4, respectively:

$$\phi_K(z, V) = V(z - L/2)/L + \vartheta_K(z) \quad (3)$$

$$\phi_{Cl}(z, V) = -V(z - L/2)/L + \vartheta_{Cl}(z) \quad (4)$$

The first term on the right side of each equation is associated with the applied voltage; because the pore is modeled as an approximately cylindrical structure of uniform radius, we assume that the applied voltage drops off linearly with respect to the position along the bilayer. $\vartheta_K(z)$ and $\vartheta_{Cl}(z)$ are the DelPhi computed potentials for $K^+$ and $Cl^-$, respectively. $D_K$ and $D_{Cl}$, the only two adjustable parameters in the curve fitting, are the ion diffusion coefficients in the channel and are determined by curve fitting 230 current-voltage points between ±150 mV for both symmetrical (N-side/C-side KCl concentrations of 1.0 M/1.0 M, 0.5 M/0.5 M, 0.24 M/0.25 M, 0.12 M/0.12 M, and 0.068 M/0.071 M) and asymmetrical (1.0 M/0.24 M, 1.1 M/0.053 M, 0.24 M/1.0 M, and 0.069 M/1.1 M) KCl concentrations using the program MLAB (Civilized Software, Bethesda,

**TABLE 3 Computed structural and physical properties of the ion channel models**

| | Model | Aggregation number | $r$ (Å)* | $P_K$[#] | $P_{Cl}$[#] | $\beta_K$[§] | $\beta_{Cl}$[§] | $\sigma_{pA}$ (pA)[¶] | $\sigma_{E_0}$ (mV)[‖] |
|---|---|---|---|---|---|---|---|---|---|
| Group 1 | T10 | 5** | 2.3 ± 0.4 | $6 \times 10^{-18}$ | $2 \times 10^{-16}$ | $5 \times 10^{16}$ | $6 \times 10^{14}$ | 2.2 | 12.7 |
| | G9 | 6 | 3.0 ± 0.3 | ≪0.1 | ≪0.1 | NA[##] | NA | NA | NA |
| | GB9 | 6 | 3.5 ± 0.4 | 0.03 | ≪0.1 | NA | NA | NA | NA |
| | T9 | 6 | 3.0 ± 0.2 | ≪0.1 | ≪0.1 | NA | NA | NA | NA |
| | T10 | 6 | 3.6 ± 0.3 | ≪0.1 | ≪0.1 | NA | NA | NA | NA |
| | T9 | 7 | 4.1 ± 0.3 | 0.1 | 0.04 | 8.0 | 6.8 | 1.3 | 8.0 |
| Group 2 | G10 | 6 | 3.8 ± 0.2 | 0.34 | 0.4 | 130 | 1.6 | 2.1 | 34 |
| | G9 | 7 | 4.6 ± 0.3 | 0.14 | 0.25 | 6.6 | 0.38 | 2.7 | 8.0 |
| | G10 | 7 | 4.8 ± 0.3 | 0.09 | 0.62 | 4.5 | 0.6 | 1.3 | 22.8 |
| | T10 | 7 | 5.2 ± 0.5 | 0.06 | 0.5 | 3.2 | 0.3 | 1.6 | 13.8 |
| | T10 | 8 | 6.8 ± 0.3 | 0.23 | 0.74 | 1.4 | 0.14 | 1.8 | 16.4 |
| Group 3 | GB10 | 6 | 4.3 ± 0.5 | 0.4 | 0.02 | 1.9 | 7.6 | 1.6 | 7.3 |
| | GM10 | 6 | 4.4 ± 0.6 | 0.49 | 0.03 | 1.4 | 8.3 | 1.6 | 6.4 |
| | GB9 | 7 | 5.3 ± 0.3 | 1.1 | 0.04 | 0.23 | 4.0 | 1.7 | 6.6 |
| | GM10 | 7 | 5.8 ± 0.4 | 1.6 | 0.015 | 1.4 | 8.3 | 2.8 | 13.5 |
| Group 4 | MD[§§] | 6 | 6.5 ± 2 | 0.2 | 0.05 | 0.9 | 1.2 | 1.3 | 9.3 |
| | GB10 | 7 | 5.9 ± 0.5 | 1.0 | 0.08 | 0.6 | 1.6 | 1.6 | 6.3 |
| | GB10 | 8 | 7.5 ± 0.2 | 0.9 | 0.15 | 0.18 | 0.6 | 1.2 | 8.1 |

*Mean and standard deviation of pore radius calculated by HOLE (Smart et al., 1996).
[#]Partition coefficient computed using Eq. 5.
[§]The ratio of the diffusion coefficients for $K^+$ or $Cl^-$ in the pore of the channel versus bulk solution determined from Eq. 2.
[¶]R.m.s.d. between the experimental *IV* data and the theoretical curve obtained from Eq. 2.
[‖]R.m.s.d. between observed reversal potentials and those from fitted *IV* curves.
**The properties of this model are representative of all pentamers.
[##]Curve-fitting not performed because of unreasonable values for $P_K$ or $P_{Cl}$.
[§§]Results obtained from the average of six structures generated by molecular dynamics (see Methods and Zhong et al., 1998).

MD). $\beta_K$ and $\beta_{Cl}$ (in Table 3) represent the ratios $D_K/D_K^{bulk}$ and $D_{Cl}/D_{Cl}^{bulk}$, respectively, and show the relationship between the computed ion diffusion coefficients in the channel and those measured in bulk water ($2 \times 10^{-5}$ cm$^2$/s for both ions). The partition coefficients of $K^+$ and $Cl^-$ from bulk into the channel pore at zero applied voltage ($P_K$ and $P_{Cl}$) were computed by numerical integration of $\vartheta_K$ and $\vartheta_{Cl}$:

$$P_{K,Cl} = L \Big/ \int_{-L/2}^{+L/2} \exp[\vartheta_{K,Cl}(z)F/RT]dz \qquad (5)$$

(for integration, the area is found by calculating the sum of the trapezoids formed by the data points). We assume that ideally, $\vartheta_K$ and $\vartheta_{Cl}$ should account completely for the partitioning of ions from bulk into the channel pore.

In Figs. 9, 10, and 12, the desolvation, Ser side chain, and backbone components to the potential energy were computed:

$$PE_i = \int_{-L/2}^{+L/2} [\vartheta_i(z)]dz/2L \qquad (6)$$

where $i$ represents desolvation, Ser side chain or backbone. The asymmetries of the individual components of the potential energy were calculated:

$$\text{Asymmetry}_i = \left( \int_{-L/2}^{0} [\vartheta_i(z)]dz/L \right) - \left( \int_{0}^{+L/2} [\vartheta_i(z)]dz/L \right) \qquad (7)$$

## RESULTS

The focus of this manuscript is to evaluate a series of static and dynamic structures to determine which features give rise to efficient conduction in this class of channels. We therefore used the general approach of Dunker (Dunker and Zaleske, 1977) to mathematically generate a series of channels based on five to eight stranded idealized coiled coils. Models with systematic variations in their helix orientations and side-chain dihedrals were generated and energy minimized. The geometric features of these models and their nomenclature are presented in Table 1. A hexameric model obtained from a molecular dynamics simulation was also evaluated. The finite-difference Poisson-Boltzmann (FDPB) methodology was then used to compute the potential profiles for the channels, from which experimental *IV* curves could be computed by using the diffusion coefficients of $K^+$ and $Cl^-$ in the pore as the only adjustable parameters.

To determine how well the various models are able to explain the experimental data (Table 3), it is necessary to determine whether the computed adjustable parameters are reasonable. Given the dimensions of the pores, we assume that the diffusion coefficients for $K^+$ and $Cl^-$ should not be greater than those in the bulk ($\beta_K$ and $\beta_{Cl}$ values less than or equal to 1). We therefore use three criteria to evaluate each model: 1) $\beta_K$ and $\beta_{Cl}$ should be less than or equal to unity; 2) the r.m.s. deviation between the computed versus the experimental *IV* curves ($\sigma_{pA}$) should approach the experimental error (±0.2 pA); and 3) the r.m.s. deviation

between the experimental and computed reversal potentials ($\sigma_{E0}$) should approach its experimental error ($\pm 1.7$ mV). Using these criteria, the models can be grouped into four categories, as shown in Table 3. One model from each category was selected and described in more detail below.

### Group 1: models with pore radii that are too small

The first group of channels shows a very small pore radius (2.8 Å average). Many models in this group provide a very reasonable fit to the experimental *IV* data, displaying both rectification and appropriate current magnitudes (Fig. 4 *B*). However, the computed values of $\beta_K$ and $\beta_{Cl}$ are unreasonably large. The computed potential profiles display a very large barrier to ion permeability (Fig. 4 *A*); the values of $P_K$ and $P_{Cl}$ predict negligible partitioning of either $K^+$ or $Cl^-$ into the pore of the T10 pentamer. Given both the small pore size and the sensitivity of an ion's image charge to the pore radius (Parsegian, 1969), this is not surprising. To compensate for this unfavorable desolvation energy, unrealistically large values for the ion diffusion coefficients in the pore are computed (as indicated by $\beta_K$ and $\beta_{Cl}$). All of the models in this group, which includes all of the pentamer models, four hexamer models, and one heptamer model, generate similarly unsatisfactory values for these parameters.

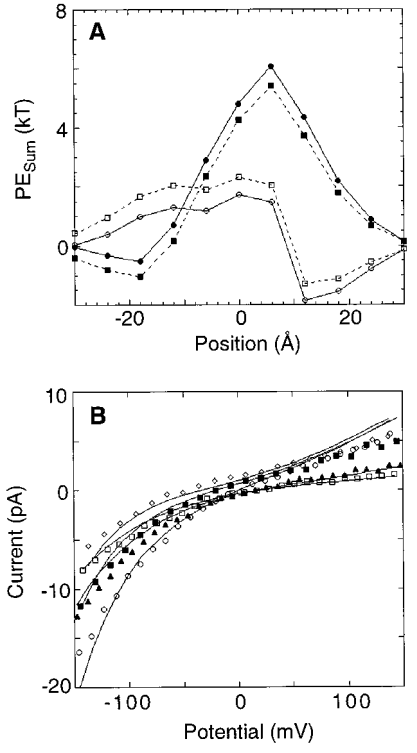


FIGURE 6 Computed potential profiles (*A*) and curves fitted to experimental *IV* data (*B*) for the GB10 hexamer model. The symbols are the same as in Fig. 4.

### Group 2: underprediction of cation selectivity

The models in group 2, with an average pore radius of 5.0 Å, have larger channels than group 1. This increase in size translates to a decrease in the magnitude of the potential energy profiles (Fig. 5 *A*). As a result, reasonable values of $P_K$ and $P_{Cl}$ are computed. However, the potential profiles for the G9 heptamer and other members of this group predict greater partitioning of $Cl^-$ into these channels than $K^+$ ($P_{Cl}$ larger than $P_K$), suggesting that they would be anion selective. To fit the *IV* data, the computed diffusion coefficients for $K^+$ are therefore inflated (as indicated by the large $\beta_K$ values) to match the cation selectivity measured experimentally. For instance, for the G10 hexamer, a $K^+$ diffusion coefficient 130 times greater than bulk is required. Furthermore, all members of this group produce poor fits to the *IV* data, as seen in the large values for $\sigma_{pA}$ and in their underprediction of rectification (Fig. 5 *B*).

### Group 3: overprediction of cation selectivity

Although the models in group 3 have radii similar to those of group 2 (4.8 Å for group 3 versus 5.0 Å for group 2), they show distinct predicted properties. Their potential profiles overpredict the cation selectivity of the channel (Fig. 6), with $P_K$ values that are on average far larger than the corresponding values for $P_{Cl}$. To compensate for this overprediction of cation permeation, the fitted diffusion coefficients for $Cl^-$ are increased 4- to 8.3-fold relative to those in bulk water.

### Group 4: experimentally consistent models

Group 4 comprises three models that provide reasonable fits to the experimental data. Fig. 7 shows the computed potential profiles and the fits to the experimental *IV* data for these three models (MD hexamer, the GB10 heptamer, and the GB10 octamer). The $P_K$ values for these models are ~10-fold greater than their $P_{Cl}$ values (4-, 6-, and 12.5-fold greater for the MD hexamer, GB10 heptamer, and GB10 octamer, respectively). The fits to experimental data for these models give experimentally reasonable values of $\beta_K$ and $\beta_{Cl}$. However, the agreement with experimental results is best for the MD structures. Only for the MD structure was the value of $\beta_K$ similar to that for $\beta_{Cl}$. Moreover, the MD ensemble of structures gave values of $\beta_K$ and $\beta_{Cl}$ that were extremely close to unity. Indeed, the full set of *IV* curves for LS3 can be fit by using the potential profile from the MD structure and no adjustable parameters ($\sigma_{pA} = \pm 1.5$ pA; $\sigma_{E0} = \pm 9.4$ mV), if one assumes that the diffusion coefficients for $K^+$ and $Cl^-$ are identical to their bulk values (Fig. 8). Finally, the effective pore radius inferred from the MD structures was in best agreement with the radius of the channel, as experimentally determined using various-sized organic cations. $Tris^+$ (with a radius of ~3.7 Å) is the largest cation known to be able to diffuse at measurable

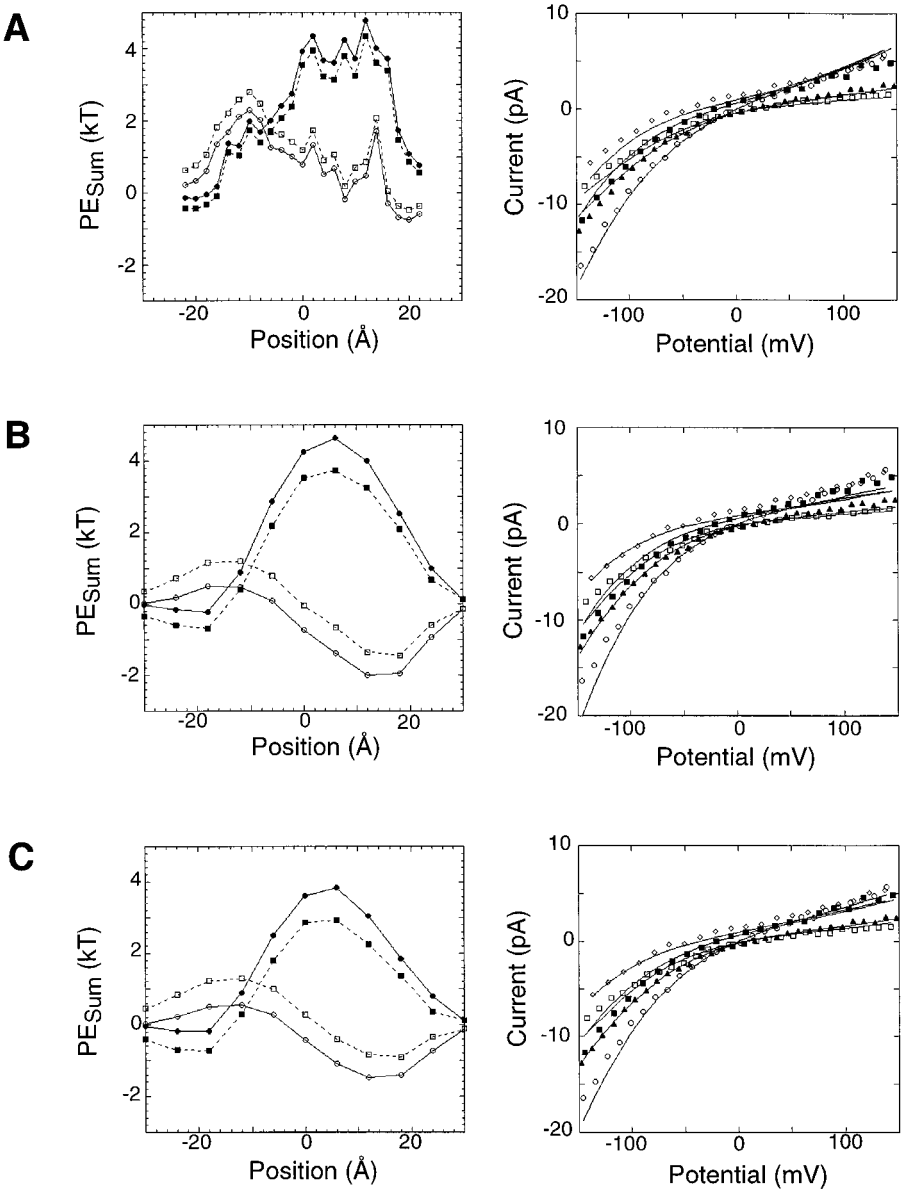


FIGURE 7 Computed potential profiles (*left*) and curves fitted to experimental *IV* data (*right*) for the MD hexamer (*A*), GB10 heptamer (*B*), and GB10 octamer (*C*) models. For the potential profiles, the potential energy (*kT*) is plotted versus the position of the permeating ion in the channel pore (Å) along the *z* axis. Potentials are shown for $K^+$ (◇, □, ○) and $Cl^-$ (●, ■, ▲) with N-side/C-side KCl concentrations of 1.1 M/0.053 M (○, ●) or 0.069 M/1.1 M (□, ■). For the plots showing curves fitted to *IV* data, the solid lines represent the fits and the symbols represent the experimental data for various N-side/C-side KCl concentrations (1.0 M/1.0 M, ○; 1.0 M/0.24 M, ■; 1.1 M/0.053 M, ◇; 0.24 M/1.0 M, ▲; 0.069 M/1.1 M, □).

rates through the channel, suggesting that the narrowest point of the pore should approach this value. The minimized structures from group 4 have very regular cylindrical shapes, with pore radii significantly greater than 4 Å. In contrast, the MD structures show much greater variability along the path of the pore, with a minimum near 4 Å.

## DelPhi-computed potential profiles

One advantage of the approach used in this study is that the potential profile for each model of LS3 is computed as the sum of three separate components—the desolvation, Ser side-chain, and backbone terms—so each component can be examined separately and related to specific structural features of the models. For a given model, the desolvation term is about the same for the $K^+$ and $Cl^-$ ions; the Ser side-chain and backbone contributions for $K^+$ and $Cl^-$ permeation are also similar in magnitude but opposite in sign. In this Results we will therefore only discuss the $K^+$ profiles, although both the $K^+$ and $Cl^-$ are used in the curve-fitting procedures.

## Desolvation component

The mean computed desolvation energies for $K^+$ in the various models are shown in Fig. 9. As expected, the radius of the channel pore has a dramatic effect on the energetic penalty for moving an ion from the bulk, high-dielectric region to the anisotropic dielectric environment of the channel pore. As the pore radius becomes larger, the desolvation energy approaches zero. Models with pore radii below 3.8 Å (including all pentamer models and four of the energy-minimized hexamer models) have large desolvation ener-

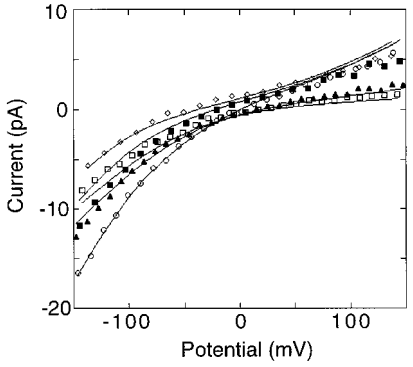


FIGURE 8 Experimental *IV* data and fitted curves for the MD hexamer model. Data were fit using zero adjustable parameters. $D_K$ and $D_{Cl}$ were assigned bulk diffusion coefficient values. The solid lines represent the fits and the symbols represent the experimental data for various N-side/C-side KCl concentrations (1.0 M/1.0 M, ○; 1.0 M/0.24 M, ■; 1.1 M/0.053 M, ◇; 0.24 M/1.0 M, ▲; 0.069 M/1.1 M, □).

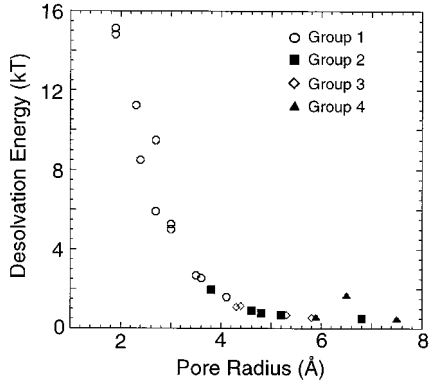


FIGURE 9 Desolvation component values for a permeating $K^+$ ion through the various ion channel models in the presence of 1.0 M/1.0 M N-side/C-side KCl concentrations. The asymmetry of the desolvation potential energy was $-0.14 \pm 0.03$ *kT*. Group 1 (○), group 2 (■), group 3 (◇), and group 4 (▲) models are shown. The estimated uncertainty from the grid positioning is 0.074*kT*.

gies, preventing effective partitioning of ions from the bath into the channel pore (Table 3).

The lack of asymmetry in the desolvation potential profiles for models with radii greater than 3.8 Å (Fig. 9) reflects the uniform cylindrical shape of the pores. The three models whose computed potential profiles give reasonable fits to the experimental data (group 4, Table 3) have pore radii above 5.9 Å. However, the T10 octamer model (group 2) has an average pore radius of 6.8 Å but provides a poor fit, indicating that the size of the pore, although important, is not sufficient for a good fit to the experimental data.

## Ser side-chain component

The mean Ser side-chain components of the potential profiles for the various models are shown in Fig. 10. In the original design of LS3, Ser was chosen as a neutral, polar residue for the lining of the pore. In this study we built different models that varied the extent to which the hydroxyl groups were exposed to solvent in the pore, as well as the specific Ser side-chain rotamer. The Ser side chains indeed appear to play a significant role in the energetics of ion permeation through the pore. Two groups of models in which the helical rotation allows maximum exposure of Ser side chains to the pore (designated GB and GM models; Table 1) show a favorable Ser side-chain component for $K^+$ permeation. The other models have unfavorable Ser side-chain/$K^+$ interaction energies, which actually predict a favorable partitioning of $Cl^-$ rather than $K^+$. In contrast, the most reasonable models (group 4) show favorable Ser side-chain interactions with $K^+$, which account for much of their cation selectivity. We observe a small degree of asymmetry in the Ser component (Fig. 10), as has been discussed previously (Mitton and Sansom, 1996). However, the magnitude of this asymmetry is much smaller than the asymmetry in the backbone component and hence does not contribute to the observed asymmetrical (rectifying) *IV* curves.

The two most favorable Ser side-chain rotamers ($g+$ and $g-$ observed in $\alpha$-helices in natural proteins (Dunbrack and Cohen, 1997; Dunbrack and Karplus, 1994; McGregor et al., 1987) were incorporated into our model study. The two rotamers showed similar favorable Ser side-chain components. The MD hexamer value represents the average of six different models taken at 6-ps intervals from a molecular dynamics simulation. As can be seen in Fig. 11, the computed Ser side-chain/$K^+$ interaction energy component for the six structures varies by up to 1*kT*. This variation is primarily due to differences in the positions of the individual helices and less to differences in the rotamers of the Ser side chains; the Ser side chains adopt a $g-$ conformation ($\chi_1 = -53 \pm 13$) in all of the MD structures. It is important again to note the level of sensitivity shown by the electro-

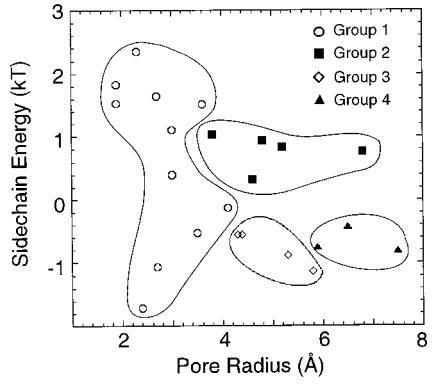


FIGURE 10 The computed energy of interaction between the Ser side chains and a permeating $K^+$ ion through the various ion channel models in the presence of N-side/C-side KCl concentrations of 1.0 M/1.0 M. The side-chain energy asymmetry was $-0.04 \pm 0.06$ *kT*. Group 1 (○), group 2 (■), group 3 (◇), and group 4 (▲) models are shown. The uncertainty estimated from grid positioning is 0.014*kT*.

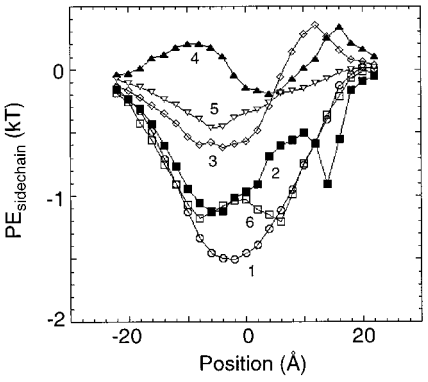


FIGURE 11 Side-chain potential energies ($kT$) for a permeating $K^+$ ion with N-side/C-side KCl concentrations of 1.0 M/1.0 M for the six structures from molecular dynamics (Zhong et al., 1998). ○, Structure 1; ■, structure 2; ◇, structure 3; ▲, structure 4; ▽, structure 5; □, structure 6. Sequential structures are 6 ps apart in the dynamics trajectory.

static calculations to the exact positioning of the Ser side chains, even for channels with pore radii as large as 5–8 Å.

### Backbone component

The backbone contribution to the computed potential profiles is shown in Fig. 12 for all models. Because the peptides are all modeled as $\alpha$-helices, the amide protons and carbonyl groups point toward the N-terminus and C-terminus, respectively. With the partial charges assigned to these atoms (see Table 2), a $K^+$ ion experiences a net positive electrostatic interaction at the N-terminal half of the model and a net negative electrostatic potential on the C-terminal half (Fig. 3 *C*). The asymmetry in the backbone component is the only significant source of asymmetry observed in the computed potential profiles and is therefore the major source of rectification in the models. Averaging over the entire length of the channel gives a value of $-0.20 \pm 0.05$, indicating that the backbone may make a small contribution to the cation selectivity. This favorable interaction between $K^+$ and the peptide backbone may arise from the tendency of the carbonyl groups to tilt away from the helical axis (Pauling et al., 1951), particularly when on the polar side of an amphiphilic $\alpha$-helix (Barlow and Thornton, 1988; Karle and Balaram, 1990).

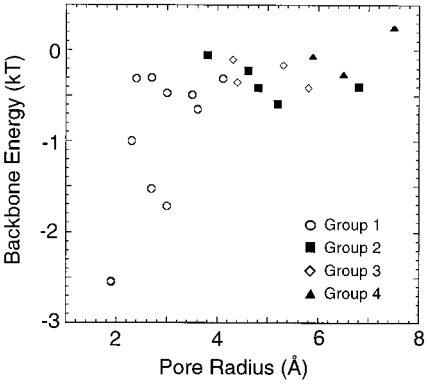


FIGURE 12 Backbone component values for a permeating $K^+$ ion through the various ion channel models in the presence of N-side/C-side KCl concentrations of 1.0 M/1.0 M. The backbone energy asymmetry was $1.19 \pm 0.06kT$ (because the N-side and C-side parts of the backbone potential for most models are approximately equal in magnitude but opposite in sign, the asymmetry value is ~1, not 0). Group 1 (○), group 2 (■), group 3 (◇), and group 4 (▲) models are shown. The uncertainty estimated from the grid positioning is $0.018kT$.

## DISCUSSION

In this manuscript we use FDPB theory to examine a series of models of LS3 that canvas a wide range of structural space. Several facts suggest that such a continuum electrostatic approach might be appropriate for the LS3 channel: 1) we have previously demonstrated that the channel has a pore radius of at least 4 Å (Lear et al., 1988). 2) Molecular dynamics calculations by Sansom (Mitton and Sansom, 1996) suggest that the relaxation times of the individual water molecules in the pore of LS3 are orders of magnitude faster than the time required for transmission of an ion through the pore. 3) Continuum electrostatic methods have been remarkably successful for the calculation of ion solvation energies (Honig et al., 1993). 4) A major energetic feature determining ion translocation rates is the dehydration energy (Parsegian, 1969); the calculation of this term is relatively insensitive to the dielectric constants of the water and protein matrix (Honig et al., 1993). Ion channels provide an important challenge for FDPB because of the extreme sensitivity of ion permeation kinetics to the structural details of the pores. In particular, we sought models that explain the permeation rates, rectification, and selectivity of LS3. Significantly, very few of the individual energy-minimized models were able to explain the experimental data, whereas the average from an ensemble of molecular dynamics structures showed excellent agreement with the data. Indeed, this ensemble was able to predict the *IV* curves with no adjustable parameters!

Our calculations indicate that the magnitude of the conduction through the LS3 channels is largely defined by the unfavorable dehydration energy associated with the transfer of an ion through the pore of the channel. This term reaches a maximum near the center of the bilayer, and only those models with internal radii greater than 3.8 Å were able to provide reasonable fits to the data. This finding is in good agreement with the size of the channel, as experimentally estimated using variously sized, permeant cations (Lear et al., 1988). This conclusion is also consistent with the recently published structure of a bacterial potassium channel, whose pore widens to almost 10 Å near the center of the channel. It is also interesting that two independently predicted models of the $M_2$ proton channel pore region show a substantial opening of the pore near the center of the bilayer (Pinto et al., 1997; Sansom et al., 1997a). In addition, our calculations indicate that models with six to eight helices best fit the data, which is close to the number of helices

inferred from the gating charge (six to seven) (Åkerfeldt et al., 1993). Thus, although there was no preconceived pore radius introduced in our theory, there was good agreement between the calculations and the experimental data.

The FDPB calculations also explain the modest (~10:1) selectivity of the LS3 channels for conduction of $K^+$. This selectivity appears to arise primarily from the interaction of the Ser side chains with the permeating ions. Interestingly, the computed energies of interaction depend on both the conformations of the Ser side chains as well as the orientation of the helices. In the models that best conform to the experimental data, we observe H-bonding between the Ser hydroxyl and the backbone carbonyl groups, as has also been described in previous MD models of LS3 (Mitton and Sansom, 1996). This arrangement positions the hydroxyl groups such that they can interact slightly better with cations than anions. However, in the absence of geometric features that stabilize a specific juxtaposition of the Ser side chains, the degree of selectivity provided by this H-bonded interaction is not great. To provide a greater degree of selectivity, it appears necessary to introduce formally charged groups (Lear et al., 1997) near the mouth of the channel, or to create a finely tuned arrangement of chelating groups within a region of smaller diameter, as in the bacterial potassium channel (Doyle et al., 1998) and gramicidin A (Roux and Karplus, 1994).

Our calculations are also able to quantitatively account for the rectification behavior of the LS3 channel, which arises from the alignment of the amide bonds in the $\alpha$-helix. Sansom and co-workers have previously noted that the dipoles associated with the Ser side chains interact favorably with the amide dipoles (Mitton and Sansom, 1996). Although this effect could, in principle, modulate the magnitude of the overall helical dipole, it is not large enough to substantially attenuate the rectification associated with the $\alpha$-helices.

In summary, we have developed methods that should be useful for the computation of *IV* curves under experimental conditions where the conductance is linear with respect to the ion concentration. This continuum theory should be applicable to single ion-occupancy channels with diameters at least as large as the LS3 pore. In addition, it will be interesting to modify this theory to evaluate channels with more restricted diameters, as the coordinates of such structures become available.

We thank Christopher Summa for computational assistance.

The work was supported in part by the Materials Research Science and Engineering Center Program of the National Science Foundation (NSF) under award number DMR96-32598, NSF grant MCB95-06900, National Institutes of Health grants GM-56423 and GM-48130, and Office of Naval Research grant N00014-95-1-0220.

## REFERENCES

Åkerfeldt, K. S., P. K. Kienker, J. D. Lear, and W. F. DeGrado. 1995. Structure and conduction mechanisms of minimalist ion channels. *In* Comprehensive Supramolecular Chemistry. Pergamon, London. 659–686.

Åkerfeldt, K. S., J. D. Lear, Z. R. Wasserman, L. A. Chung, and W. F. DeGrado. 1993. Synthetic peptides as models for ion channel proteins. *Acc. Chem. Res.* 26:191–197.

Barlow, D. J., and J. M. Thornton. 1988. Helix geometry in proteins. *J. Mol. Biol.* 201:601–619.

Betz, S. F., and W. F. DeGrado. 1996. Controlling topology and native-like behavior of de novo-designed peptides: design and characterization of antiparallel four-stranded coiled coils. *Biochemistry.* 35:6955–6962.

Bormann, J., O. P. Hamill, and B. Sakmann. 1987. Mechanism of anion permeation through channels gated by glycine and $\gamma$-aminobutyric acid in mouse cultured spinal neurones. *J. Physiol. (Lond.).* 385:243–286.

Chen, D. P., V. Barcilon, and R. S. Eisenberg. 1992. Constant fields and constant gradients in open ionic channels. *Biophys. J.* 61:1372–1393.

Chen, D. P., J. D. Lear, and R. S. Eisenberg. 1997. Permeation through an open channel. Poisson-Nernst-Planck theory of a synthetic ion channel. *Biophys. J.* 72:97–116.

Cohen, B. N., C. Labarca, N. Davidson, and H. A. Lester. 1992. Mutations in M2 alter the selectivity of the mouse nicotinic acetylcholine receptor for organic and alkali metal cations. *J. Gen. Physiol.* 100:373–400.

Cortis, C. M., and R. A. Friesner. 1997. Numerical solution of the Poisson-Boltzmann equation using tetrahedral finite-element meshes. *J. Comput. Chem.* 18:1591–1608.

Crick, F. H. C. 1953. The packing of alpha-helices: simple coiled-coils. *Acta Crystallogr.* 6:689–697.

Dauber-Osguthorpe, P., V. A. Roberts, D. J. Osguthorpe, J. Wolff, M. Genest, and A. T. Hagler. 1988. Structure and energetics of ligand binding to proteins: *Escherichia coli* dihydrofolate reductase-trimethoprim, a drug-receptor system. *Proteins Struct. Funct. Genet.* 4:31–47.

Dieckmann, G. R. 1995. Use of metal-binding de novo-designed $\alpha$-helical peptides in the study of metalloprotein structures. PhD thesis. University of Michigan Press, Ann Arbor, MI. 295.

Dieckmann, G. R., and W. F. DeGrado. 1997. Modeling transmembrane helical oligomers. *Curr. Opin. Struct. Biol.* 7:486–494.

Doyle, D. A., J. M. Cabral, R. A. Pfuetzner, A. Kuo, J. M. Gulbis, S. L. Cohen, B. T. Chait, and R. MacKinnon. 1998. The structure of the potassium channel: molecular basis of $K^+$ conduction and selectivity. *Science.* 280:69–77.

Dunbrack, R. L., Jr., and F. E. Cohen. 1997. Bayesian statistical analysis of protein side-chain rotamer preferences. *Protein Sci.* 6:1661–1681.

Dunbrack, R. L., Jr., and M. Karplus. 1994. Conformational analysis of the backbone-dependent rotamer preferences of protein sidechains. *Nature Struct. Biol.* 1:334–340.

Dunker, K., and D. J. Zaleske. 1977. Stereochemical considerations for constructing alpha-helical proteins with particular application to membrane proteins. *Biochem. J.* 163:45–57.

Dwyer, T. M., D. J. Adams, and B. Hille. 1980. The permeability of the endplate channel to organic cations in frog muscle. *J. Gen. Physiol.* 75:469–492.

Fatima-Shad, K., and P. H. Barry. 1993. Anion permeation in GABA- and glycine-gated channels of mammalian cultured hippocampal neurons. *Proc. R. Soc. Lond. (Biol.).* 253:69–75.

Gilson, M. K., K. A. Sharp, and B. Honig. 1988. Calculating the electrostatic potential of molecules in solution: method and error assessment. *J. Comput. Chem.* 9:327–335.

Hao, Y., M. R. Pear, and D. D. Busath. 1997. Molecular dynamics study of free energy profiles for organic cations in gramicidin A channels. *Biophys. J.* 73:1699–1716.

Hille, B. 1992. Ionic Channels of Excitable Membranes. Sinauer Associates, Sunderland, MA.

Holst, M., and F. Saied. 1993. Multigrid solution of the Poisson-Boltzmann equation. *J. Comput. Chem.* 14:105–113.

Honig, B., K. Sharp, and A.-S. Yang. 1993. Macroscopic models of aqueous solutions: biological and chemical applications. *J. Phys. Chem.* 97:1101–1109.

Imoto, K. 1993. Ion channels: molecular basis of ion selectivity. *FEBS Lett.* 325:100–103.

Jorgensen, W. L., and J. Tirado-Rives. 1988. The OPLS potential functions for proteins. Energy minimizations for crystals of cyclic peptides and crambin. *J. Am. Chem. Soc.* 110:1657–1666.

Karle, I. L., and P. Balaram. 1990. Structural characteristics of $\alpha$-helical peptide molecules containing Aib residues. *Biochemistry.* 29: 6747–6756.

Kienker, P. K., W. F. DeGrado, and J. D. Lear. 1994. A helical-dipole model describes the single-channel current rectification of an uncharged peptide ion channel. *Proc. Natl. Acad. Sci. USA.* 91:4859–4863.

Kienker, P. K., and J. D. Lear. 1995. Charge selectivity of the designed uncharged peptide ion channel Ac-$(LSSLLSL)_3$-$CONH_2$. *Biophys. J.* 68:1347–1358.

Kohn, W. D., C. T. Mant, and R. S. Hodges. 1997. Alpha-helical protein assembly motifs. *J. Biol. Chem.* 272:2583–2586.

Lear, J. D., J. P. Schneider, P. K. Kienker, and W. F. DeGrado. 1997. Electrostatic effects on ion selectivity and rectification in designed ion channel peptides. *J. Am. Chem. Soc.* 119:3212–3217.

Lear, J. D., Z. R. Wasserman, and W. F. DeGrado. 1988. Synthetic amphiphilic peptide models for protein ion channels. *Science.* 240: 1177–1181.

McGregor, M. J., S. A. Islam, and M. J. E. Sternberg. 1987. Analysis of the relationship between side-chain conformation and secondary structure in globular proteins. *J. Mol. Biol.* 198:295–310.

Mitton, P., and M. S. P. Sansom. 1996. Molecular dynamics simulations of ion channels formed by bundles of amphipathic $\alpha$-helical peptides. *Eur. Biophys. J.* 25:139–150.

Nicholls, A., K. A. Sharp, and B. Honig. 1991. Protein folding and association: insights from the interfacial and thermodynamic properties of hydrocarbons. *Proteins Struct. Funct. Genet.* 11:281–296.

Parsegian, A. 1969. Energy of an ion crossing a low dielectric membrane: solutions to four relevant electrostatic problems. *Nature.* 221:844–846.

Parsegian, V. A. 1975. Ion-membrane interactions as structural forces. *Ann. N.Y. Acad. Sci.* 264:161–174.

Pauling, L., R. B. Corey, and H. R. Branson. 1951. The structure of proteins: two hydrogen-bonded helical configurations of the polypeptide chain. *Proc. Natl. Acad. Sci. USA.* 37:205–211.

Pinto, L. H., G. R. Dieckmann, C. S. Gandhi, C. G. Papworth, J. Braman, M. A. Shaughnessy, J. D. Lear, R. A. Lamb, and W. F. DeGrado. 1997. A functionally defined model for the M-2 proton channel of influenza A virus suggests a mechanism for its ion selectivity. *Proc. Natl. Acad. Sci. USA.* 94:11301–11306.

Rashin, A. A., and B. Honig. 1985. Reevaluation of the Born model of ion hydration. *J. Phys. Chem.* 89:5588–5593.

Roux, B., and M. Karplus. 1994. Molecular-dynamics simulations of the gramicidin channel. *Ann. Rev. Biophys. Biomol. Struct.* 0023:731–761.

Sansom, M. S. P., I. D. Kerr, G. R. Smith, and H. S. Son. 1997a. The influenza A virus M2 channel: a molecular modeling and simulation study. *Virology.* 233:163–173.

Sansom, M. S. P., G. R. Smith, C. Adcock, and P. C. Biggin. 1997b. The dielectric properties of water within model transbilayer pores. *Biophys. J.* 73:2404–2415.

Sather, W. A., J. Yang, and R. W. Tsien. 1994. Structural basis of ion channel permeation and selectivity. *Curr. Opin. Neurobiol.* 4:313–323.

Sharp, K. A., R. Friedman, V. Misra, J. Hecht, and B. Honig. 1995. Salt effects on polyelectrolyte-ligand binding: comparison of Poisson-Boltzmann, and limiting law/counterion binding models. *Biopolymers.* 36:245–262.

Sharp, K. A., and B. Honig. 1990. Electrostatic interactions in macromolecules: theory and applications. *Annu. Rev. Biophys. Biophys. Chem.* 19:301–332.

Shen, L., R. E. Bruccoleri, S. Krystek, and J. Novotny. 1996. Factors influencing accuracy of computer-built models: a study based on leucine zipper GCN4 structure. *Biophys. J.* 70:1096–1104.

Sitkoff, D., D. J. Lockhart, K. A. Sharp, and B. Honig. 1994. Calculation of electrostatic effects at the amino terminus of an alpha helix. *Biophys. J.* 67:2251–2260.

Smart, O. S., J. G. Neduvelil, X. Wang, B. A. Wallace, and M. S. P. Sansom. 1996. HOLE: a program for the analysis of the pore dimensions of ion channel structural models. *J. Mol. Graph.* 14:354–360.

Smith, G. R., and M. S. P. Sansom. 1997. Molecular dynamics study of water and $Na^+$ ions in models of the pore region of the nicotinic acetylcholine receptor. *Biophys. J.* 73:1364–1381.

Weiss, M. S., A. Kreusch, E. Schiltz, U. Nestel, W. Welte, J. Weckesser, and G. E. Schulz. 1991. The structure of porin from *Rhodobacter capsulatus* at 1.8 Å resolution. *FEBS Lett.* 280:379–382.

Weiss, M. S., and G. E. Schulz. 1992. Structure of porin refined at 1.8 Å resolution. *J. Mol. Biol.* 227:493–509.

Woolfson, D. N., and T. Alber. 1995. Predicting oligomerization states of coiled coils. *Protein Sci.* 4:1596–1607.

Woolley, G. A., P. C. Biggin, A. Schultz, L. Lien, D. C. J. Jaikaran, J. Breed, K. Crowhurst, and M. S. P. Sansom. 1997. Intrinsic rectification of ion flux in alamethicin channels: studies with an alamethicin dimer. *Biophys. J.* 73:770–778.

Yool, A. J., and T. L. Schwartz. 1991. Alteration of ionic selectivity of a $K^+$ channel by mutation of the H5 region. *Nature.* 349:700–704.

Zhong, Q., P. B. Moore, D. M. Newns, and M. L. Klein. 1998. Molecular dynamics study of the LS3 voltage-gated ion channel. *FEBS Lett.* 427:267–274.